



Finite element and experimental study of the residual stresses in 2024-T3 Al alloy treated via single toroidal roller burnishing

G. V. Duncheva¹ · J. T. Maximov¹ · A. P. Anchev¹ · V. P. Dunchev¹ · T. P. Atanasov¹ · Jiri Capek²

Received: 8 July 2020 / Accepted: 15 December 2020 / Published online: 8 January 2021
© The Brazilian Society of Mechanical Sciences and Engineering 2021

Abstract

This article presents the outcomes of finite element (FE) simulations and X-ray stress measurements of residual stresses in high-strength 2024-T3 Al alloy introduced via the single toroidal roller burnishing (STRB) process. In terms of the deforming toroidal roller geometry, STRB is particularly suitable for deep rolling. A 3D FE model was developed using the flow stress concept, and the actual STRB kinematics was simulated to evaluate both hoop and axial residual stresses. The FE model was validated through a comparison of FE and X-ray residual stress distributions. The effects of the burnishing force, feed rate, and number of passes on the residual hoop and axial stresses were studied. It was established that increasing the feed rate leads to a decrease in the residual hoop stresses and an increase in the residual axial stresses. The greater burnishing force increases the compressive zone depth and only slightly increases the surface residual stresses. The FE and X-ray stress analyses confirm the effectiveness of STRB of 2024-T3 Al alloy to introduce significant residual compressive axial and hoop stresses.

Keywords 2024-T3 Al alloy · Roller burnishing · Deep rolling · Residual stresses · X-ray stress analysis · FEM

List of symbols

A_5	Elongation	v	Burnishing velocity
A	Amplitude	α_{ij}	Back-stress tensor
B	Amplitude	$\bar{\epsilon}_p$	Equivalent plastic strain
C	Kinematic hardening modulus	ϕ	Roller rotation angle
D	External diameter of the toroidal deforming roller	γ	Rate of decrease in C
d	Workpiece diameter	ν	Poisson's ratio
d_p	Depth of penetration	$\theta(\theta_0)$	Central angles of the workpiece modeled portion
E	Young's modulus	σ^0	Equivalent stress
f	Feed rate	σ_a	Stress amplitude
F_b	Burnishing force	σ_{ij}	Stress tensor
n	Number of passes	σ_{-1}	Fatigue limit for symmetrical cycle
N	Number of cycles to failure	σ_u	Ultimate stress
r	Radius of the toroid of the toroidal deforming roller	σ_Y	Yield limit
R	Cycle asymmetry coefficient	σ_t^{res}	Residual hoop stress
t_{step}	One cycle time	σ_z^{res}	Residual axial stress
		ω	Angular velocity
		ψ	Transverse contraction

Abbreviations

CNC	Computer numerical control
DR	Deep rolling
FE	Finite element
HBB	Hydrostatic ball burnishing
LPB	Low plasticity burnishing
MST	Mechanical surface treatment
RB	Roller burnishing

Technical Editor: Lincoln Cardoso Brandao.

✉ G. V. Duncheva
duncheva@tugab.bg

¹ Technical University of Gabrovo, 5300 Gabrovo, Bulgaria

² Czech Technical University in Prague, Prague, Czech Republic

SB	Slide burnishing
SRB	Single roller burnishing
STRB	Single toroidal roller burnishing

1 Introduction

High-strength aluminum alloys, including 2024-T3, are appropriate materials for aerospace and automotive applications because of their high strength to weight ratio, high fatigue resistance, corrosion resistance, and fabricability. In most of these applications, the fatigue is critical to the strength and operational safety of the metal components. The fatigue cracks originate and develop mainly in the surface layers of the elements where the highest working stresses occur. Therefore, the fatigue strength of a structural component depends on the complex properties of the surface layers, defining its surface integrity (SI). To increase fatigue life, low roughness, increased microhardness, residual compressive stresses, and modified microstructure in the surface layers are necessary. Mechanical surface treatment (MST) processes based on surface severe plastic deformation are particularly suitable to provide the desired SI in the surface layers. As a result, the material undergoes strain hardening.

The static MST processes, known as burnishing processes, are appropriate for rotary elements because their parameters can be controlled in correlation with the desirable SI. Depending on the tangential contact between the deforming element and surface being treated, two types of processes exist: roller (ball) burnishing and slide burnishing (SB) [1]. In general, the burnishing processes with rolling contact have a more practical application. Using only this type of contact, Ecoroll classifies two types of burnishing processes according to the desired SI in correlation with the operating behavior: roller burnishing (RB) and deep rolling (DR) [2]. The RB process is primarily aimed to achieve a smoothing effect as the roughness is reduced considerably ($R_a \leq 0.2 \mu\text{m}$). In the DR process, the focus is on cold work and the creation of compressive residual stresses in the surface layers, as the smoothing is an accompanying effect. Therefore, the DR concept is suitable for dynamically loaded metal components. DR leads to two positive effects: micro- and macro-effect [3, 4]. The micro-effect is expressed in the microstructure modification. The macro-effect includes the creation of a deep zone with useful residual compressive macro-stresses in the surface and subsurface layers. The micro-effect of the DR process is less pronounced in comparison with SB, owing to the smaller equivalent plastic deformation of the surface layers (the thermal effect due to the DR process is negligibly small). This difference in the manifestation of the micro-effect is more pronounced for aluminum alloys, because of the large amount of heat generated by SB. Therefore, the main result of fatigue life

enhancement in aluminum alloys via DR is a macro-effect. The DR process is implemented using the following basic methods: hydrostatic ball burnishing (HBB), low plasticity burnishing (LPB), and single roller burnishing (SRB). Although physically, the LPB corresponds to the HBB, the essence of the LPB process is different. The fundamental goal of LPB is to create a zone of significant compressive residual stresses with minimum cold work and thus to minimize the effect of residual stresses relaxation due to mechanical or thermal overloading.

SRB is implemented with a cylindrical, conical, or toroidal roller. SRB is especially suitable for the finishing of rotary elements owing to the following advantages: easy implementation on conventional and CNC lathes; a low value for cost/quality ratio; the need for relatively simple devices; the possibility for easy control of the process when the deforming force is applied through an elastic system. In terms of the role of the contact zone between the deforming roller and the treated surface, the single toroidal roller burnishing (STRB) method is particularly suitable to implement DR. A toroidal roller is used as a deforming element. A principle scheme of this method is shown in Fig. 1. This technique can be used in automotive, aircraft, oil, gas industries, and machine construction, for treatment of external rotary surfaces of axles, shafts, collar pins, piston rods, valve stems, and other. For example, a typical application for aluminum shafts is for linear bearings.

As a whole, the STRB process has been studied in a limited number of publications [5–8]. Borkar et al. [5] examined the roughness and microhardness in Inconel 718 high-strength alloy as a function of the process parameters. Residual stress distribution in EA4T steel railway axles, introduced via a DR process, was studied by Hassani-Gangaraj et al. [6], using X-ray diffraction and hole drilling techniques. Dwivedi et al. [7] established that burnishing

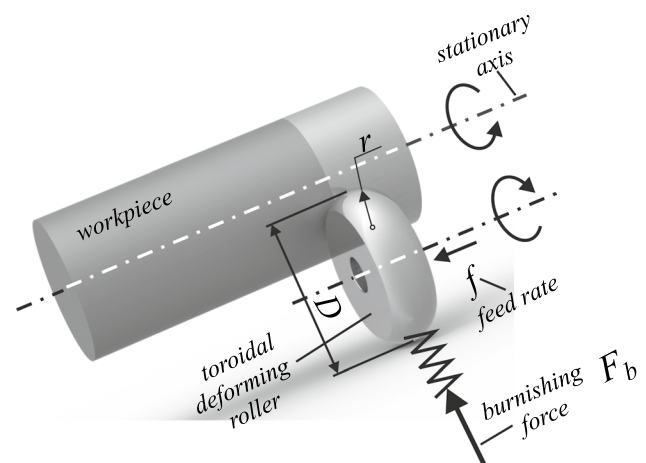


Fig. 1 STRB: principle scheme

A356/5%SiC metal matrix composite specimens improve the tensile strength, hardness, and ductility. Focusing on the residual stresses, Perenda et al. [8] experimentally and, via dynamic explicit simulations, investigated DR of high-strength TORKA steel torsion bars. In a 3D finite element (FE) model, the burnishing force was calculated using the measurements of the rolling pressure. A combined isotropic and kinematic hardening material model was used, based on the cyclic characteristics of the material.

The present study examines the hoop and axial residual stresses (Fig. 2) in high-strength 2024-T3 Al alloy introduced via STRB. For a complete and realistic assessment of the residual stresses, a combined approach is needed, including FE simulations and X-ray diffraction stress analysis. The experimental approach to the measurement of the residual macro-stresses introduced via DR is most often based on X-ray diffraction [9–11] and hole drilling [12–14] techniques. The residual stress measurement via X-ray diffraction is more reliable, but this technique is too expensive and time-consuming. From this point of view, the numerical simulations are effective for an in-depth investigation of the strained and stressed state in the surface layers after burnishing.

Different strategies exist for building FE models of the burnishing processes. In 2D FE models, the interaction between the workpiece and deforming ball (roller) is simulated under plane strain conditions. As a result, the actual contact of the ball/roller on the cylinder is transformed into a linear contact cylinder on a plane. Besides realistic boundary conditions, the chosen material constitutive model in the FE models is crucial for reliable prediction of the residual stresses. In the burnishing processes, the surface layer behavior differs significantly from that of the bulk material, owing to the presence of large plastic deformations, technological heredity, and other effects. Therefore, the flow stress concept is used to define the stress–strain dependence in the plastic field for the surface layers [3, 15–19].

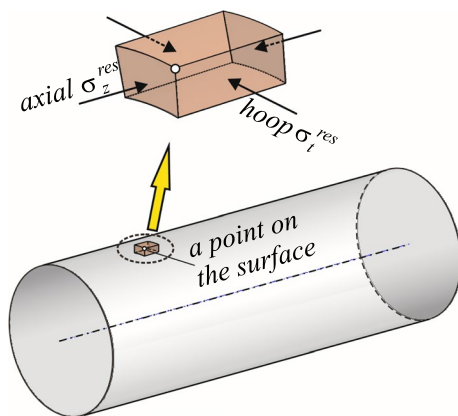


Fig. 2 Examined residual stress components

A procedure involving an instrumented indentation test and inverse FE analysis was performed in [16, 19, 20] to realistically define of the flow stress for DR simulations. Based on this procedure and using a 2D FE model, the residual stresses were investigated in AISI 1042 carbon steel [21] and MgCa0.8 biomaterial [22] cylindrical specimens subjected to HBB. Sayahi et al. developed 2D and 3D FE models of the HBB of cylindrical specimens using an isotropic hardening material model for Ti6Al7Nb alloy [23]. Comparing the numerical simulation results for the residual stress profile with experimental data obtained via X-ray diffraction measurement, the authors recommend the 3D model. A 3D FE model of the LPB process was simulated with interaction between a deformable solid ball and a plate with rolling friction contact using a rate and temperature-dependent material constitutive model [24–26]. However, the authors developed the material constitutive model differently (with the Johnson-Cook hardening model based on the bulk material [24, 25] and an indentation test using non-linear kinematic and isotropic hardening [26]). In a similar strategy, Aldrine et al. [27] developed a 3D FE model for the investigation of the residual stresses in 2024-T351 and 7075-T651 high-strength Al alloys plates subjected to LPB. The authors defined the material constitutive model with a bilinear tensile curve obtained for the bulk material and a bilinear isotropic hardening model. Balland et al. [28] developed a 3D FE model for the study of SRB (with a cylindrical roller) of 11SMn30 high-carbon steel cylindrical specimens. The authors used an anisotropic hardening material model based on Rastegaev-type geometry compression tests. In the FE model, the inversion method was used with respect to the actual method kinematics, and the workpiece rotation was transformed to the deforming roller. The proposed model was validated by comparing the numerical results for the residual axial and hoop stresses with those experimentally obtained via X-ray diffraction measurement. Beghini et al. [29] experimentally and through FE simulations investigated the DR of high-strength 7075-T6 aluminum alloy using a carbide roller tool. Focusing on the residual stress profile, a parametric analysis was performed with different combinations of the burnishing force and feed rate.

The literary survey shows that there are no publications devoted to the study of the residual stresses introduced via the STRB process in high-strength 2024-T3 alloys. An exception is a study that use FE modeling based on simplified kinematics of the STRB process and optimized the axial residual stress distribution in cylindrical specimens made of this aluminum alloy [30].

The main purpose of this study is to assess the possibilities of STRB to introduce both axial and hoop residual compressive stresses in high-strength 2024-T3 Al alloy. A suitable FE model of the STRB was created, and X-ray diffraction stress analysis was carried out.

2 Methods of study

2.1 Finite element method

2.1.1 Aim

The prevailing view is that the useful macro-effect introduced in rotational components subjected to cyclic bending depends primarily on the axial residual stresses. Because of this, in several 2D and 3D FE models, the burnishing process is simulated by simplified kinematics, which allows for relatively reliable predictions of only the axial residual stresses [3, 15–22, 30]. On the other hand, the fatigue tests confirm that the fatigue crack front in rotating components develops in arbitrary directions that do not coincide with their cross sections. Therefore, the fatigue behavior of the components depends on both the axial and hoop residual stress distributions. The purpose of the numerical simulations was to evaluate the effect of the burnishing force in correlation with the feed rate on the axial and hoop residual stress distributions in 2024-T3 Al alloy specimens subjected to STRB. To achieve this, a 3D FE model was developed, and the actual kinematics of the studied process was simulated.

2.1.2 Material characteristics

2.1.2.1 Deforming roller The deforming toroidal roller is made of hardened high-strength tool steel. The roller was modeled as a perfectly rigid body because its hardness is much higher than the workpiece surface layer.

2.1.2.2 Workpiece The chemical composition and the mechanical characteristics of the 2024-T3 Al alloy were established by us at our Testing of Metals Laboratory. In order to identify the type of material, Table 1 shows the chemical composition obtained by us as well as the chemical composition of 2024-T3 AA, according to ASM Aerospace Specification Metals Inc. The comparison shows that the alloy we use actually belongs to the group of high-strength 2024-T3 alloys. The comparison shows that the alloy we use actually belongs to the group of high-strength 2024-T3 Al alloys. Using tensile tests (at room temperature) on specimens with diameter $d = 6$ mm and base of $6d$, the following material characteristics were determined: yield strength

$\sigma_Y = 348$ MPa, tensile strength $\sigma_u = 501$ MPa, elongation $A_5 = 10.4\%$, and transverse contraction $\psi = 33\%$.

2.1.3 Material constitutive model of the workpiece surface layer

The elastic–plastic rate-independent behavior of the workpiece modeled portion was assigned. Young’s modulus and Poisson’s ratio are, respectively, $E = 72,000$ MPa and $\nu = 0.33$. The surface layer constitutive model of the aluminum alloy was defined per the flow stress concept [30]. The flow stress model of the workpiece surface and sub-surface layers in the plastic field was obtained as follows [15–17]:

$$\sigma = \sigma_Y \left(1 + \frac{E}{\sigma_Y} \bar{\epsilon}_p \right)^n, \tag{1}$$

where σ is the flow stress, σ_Y is the yield limit, E is the Young’s modulus, $\bar{\epsilon}_p$ is the plastic strain, and n defines the strain hardening for an one-dimensional stressed state. From the procedure involving an instrumented indentation test and subsequent inverse FEM analysis, the following constants in Eq. (1) were obtained [30]: $\sigma_Y = 310$ MPa and $n = 0.09$. On the other hand, the surface layer points are subjected to cyclic hardening, which leads to deformation anisotropy. This effect was taken into account by defining nonlinear kinematic hardening:

$$\dot{\alpha}_{ij} = \frac{C}{\sigma^0} \sigma_{ij}^a \dot{\epsilon}_p - \gamma \alpha_{ij} \dot{\epsilon}_p, \tag{2}$$

where σ^0 is an equivalent stress defining the yield surface size, with initial size $\sigma|_0 = \sigma_Y$ (assuming that σ^0 is valid for all possible stressed states and loading paths); $\sigma|_0$ is the equivalent stress defining the size of the yield surface at zero equivalent plastic strain $\bar{\epsilon}_p$; $\sigma_{ij}^a = \sigma_{ij} - \alpha_{ij}$ is the active stress tensor; σ_{ij} is the stress tensor; α_{ij} is the back-stress tensor; C is the initial kinematic hardening modulus; γ is a coefficient defining the rate at which the kinematic hardening modulus decreases as equivalent plastic strain increases.

The burnishing process causes cyclic loading in the vicinity of a point on the surface of the treated workpiece. As a result, deformation anisotropy occurs. The latter is a result from arising stresses from type-II (microstresses) due to change of the material structure, caused by severe plastic

Table 1 2024-T3 aluminum alloy chemical composition

	Si%	Fe%	Cu%	Mn%	Mg%	Zn%	Cr%	Ti	Other	Al%
Obtained by us	0.58	0.38	3.31	0.82	1.53	0.0624	0.0365	0.13	0.12	92.031
According to ASM*	max 0.5	max 0.5	3.8–4.9	0.3–0.9	1.2–1.8	max 0.25	max 0.1	max 0.15	max 0.15	90.7–94.7

*ASM Aerospace Specification Metals Inc.

deformation. The microstresses are described in view of the macro approach with symmetric tensor, known as backstress tensor α_{ij} . For the surface layer of the 2024-T3 AA, the magnitudes of the initial kinematic hardening modulus C and γ coefficient are, respectively, $C = 2125.84$ MPa and $\gamma = 15.45$. These values were obtained on the basis of Eq. (1), using the methodology described in [31].

2.1.4 3D FE model

A 3D FE model was developed using Abaqus CAE 2018 (Fig. 3). In accordance with the results obtained from the optimization of the process studied in [30], the simulations were performed with the following constant geometric parameters of the toroidal roller: radius of the toroid $r = 2$ mm and outer diameter $D = 26$ mm. The workpiece diameter was $d = 22$ mm. The burnishing process was simulated using displacement control of the deforming toroidal roller. A preliminary FE analysis established the interdependence between the burnishing force and depth of penetration. The variable parameters, according to the numerical simulations, are shown in Table 2.

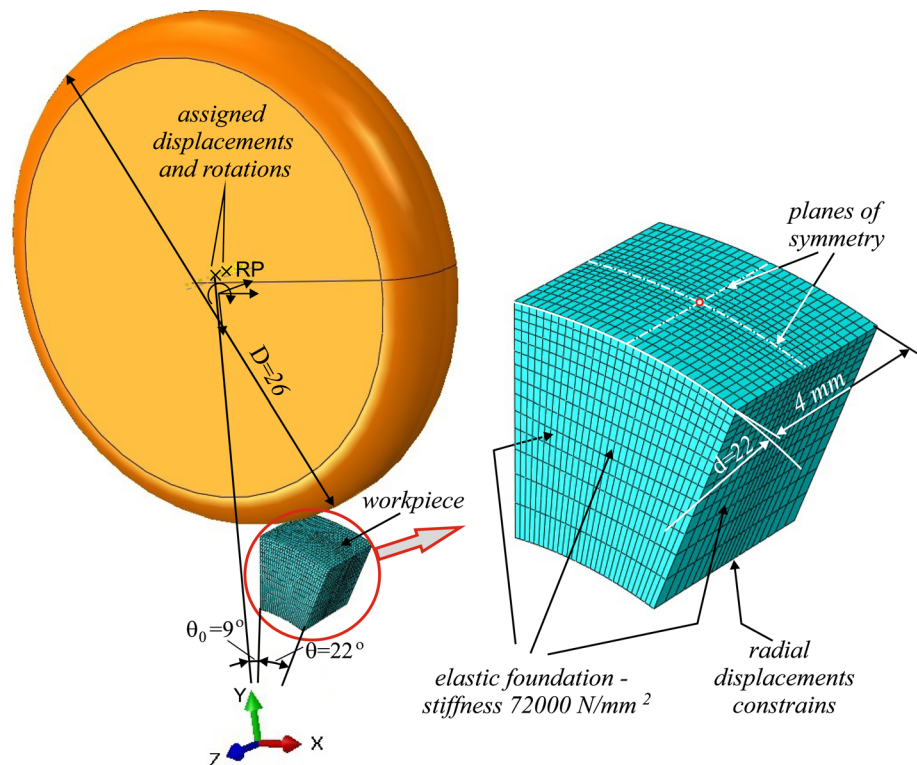
The burnishing process was simulated to investigate the feed rate impact on the residual stresses with nine identical toroidal rollers acting on the workpiece. The rollers were modeled as perfectly rigid bodies and were positioned in the axial direction at distances equal to the corresponding feed rate value. The motions of each roller were identical,

Table 2 Variable parameters in numerical simulations

No.	Burnishing force F_b , N	Depth of penetration d_p , mm	Feed rate f , mm/rev
1	800	0.0426	0.05
2			0.08
3			0.11
4	1200	0.07	0.05
5			0.08
6			0.11

defaced in the total analysis time with a value corresponding to the duration of one cycle. Because of the relatively small contact area (about 0.8×1.2 mm²) between the deforming diamond and the surface being burnished, it is assumed that the deforming impact is independent of the outer boundaries of the workpiece. The interaction of the unmodeled portion of the workpiece with the modeled portion was taken into account by assigning an elastic foundation contact with a coefficient equal to Young's modulus to all surfaces except the outer cylindrical surface (Fig. 3). Therefore, a workpiece sector with a relatively small length was modeled. All simulations were performed with the same workpiece mesh, which was refined in the contact area (Fig. 3). A total of 9765 nodes and 8400 linear hexahedral FEs of type C3D8R were used to model the workpiece. A normal and tangential mechanical contact

Fig. 3 3D FE model of STRB process



with a friction coefficient of 0.1 was assigned between the rollers and the workpiece.

In the 3D FE model, the inversion method with respect to the roller–workpiece system was used. As a result, the workpiece was stationary, and an additional angular velocity was applied to the rollers. For this purpose, the inner cylindrical surface of the workpiece was fixed in the radial direction. In fact, the trajectory of the center of the contact area between the toroidal roller and the workpiece was a screw line with a step equal to the feed rate f . The toroidal roller helical motion with respect to the fixed workpiece was defined as three translations along the three axes, and one rotation about the workpiece axis (z -axis) was assigned to the respective Reference Points (Fig. 3). Because the trajectory of each Reference Point in the xy plane is a circle, the translations of these Reference Points along x - and y -axes, respectively, were set by periodic time curves. The equations in parametric form (with time parameter t) of these curves define a central circle:

$$x_{RP} = B \sin \omega t, \quad y_{RP} = -A + A \cos \omega t, \quad (3)$$

where $A = B = \frac{d}{2} + \frac{D}{2} - d_p$ is the amplitudes, $\omega = \frac{(\theta+2\theta_0)\pi}{t_{step} 180}$ is the transfer angular velocity, θ and θ_0 (in degrees) are the central angles of the workpiece modeled portion (see Fig. 2), $t_{step} = \frac{A(\theta+2\theta_0)\pi}{v 180}$ is the one cycle time, and v is the burnishing velocity.

The roller rotation angle around z -axis was set by a tabular function that is proportional to t_{step} with the maximum value:

$$\phi = \frac{A}{0.5D}, \text{ rad} \quad (4)$$

The axial displacement of the toroidal roller (along the z -axis) is defined by a tabular function that is proportional to the feed rate f .

2.2 Experiment

2.2.1 Experimental setup

A special burnishing device (Fig. 4) was designed and manufactured to conduct the STRB process. The device was adapted for machining rotating components on both conventional and CNC lathes. A linear law of the burnishing force change F_b ranging from 400 to 1400 N was applied using a screw cylindrical spring. The burnishing device was equipped with toroidal rollers having the same maximum diameter ($D = 26$ mm), but with various toroidal radii.

2.2.2 X-ray residual stress measurement

The X-ray diffraction analysis measured the surface hoop σ_t^{res} and axial σ_z^{res} residual stresses in the cylindrical specimens with diameter $d = 20$ mm and length 30 mm. Different conditions were applied to each specimen to make a comparative assessment of the residual stresses. The parameters of the specimens according to the finishing treatment are shown in Table 3. The burnished specimens received the same feed rate and burnishing velocity $f = 0.05$ mm/rev and $v = 63$ m/min, respectively.

The X-ray diffraction measurements were performed at the Czech Technical University in Prague and carried out on a vertical θ/θ X'Pert PRO MPD diffractometer with a pin-hole collimator 0.5×1.0 mm² in the primary beam. The specimens were positioned at the required locations by combining a versatile positioning system with six degrees of freedom with laser triangulation for precise surface position determination with an accuracy of approximately ± 5 μ m. Since the effective penetration depth of the $CrK\alpha$ radiation into the investigated alloy was only approximately 8 μ m, a biaxial state of stress was assumed. The “sin 2ψ ” method with a least-squares fitting procedure was used to evaluate the {311} planes for the filtered $CrK\alpha$ radiation,

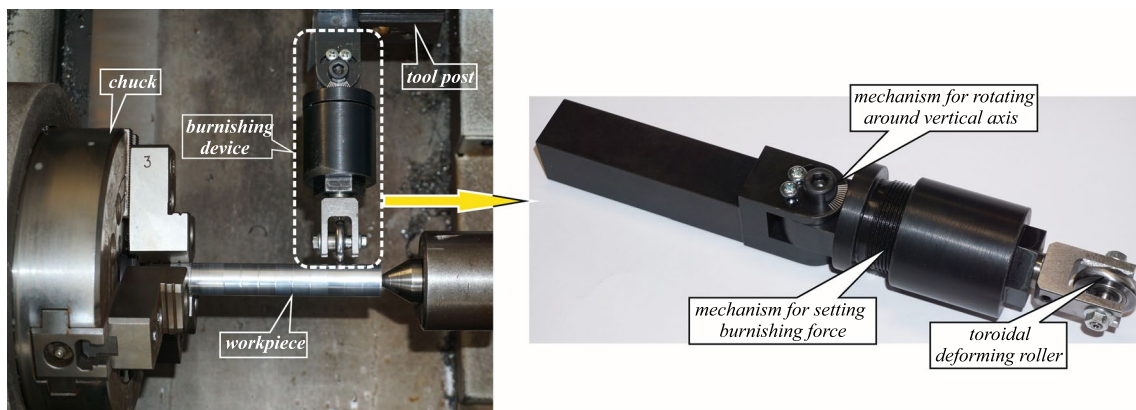


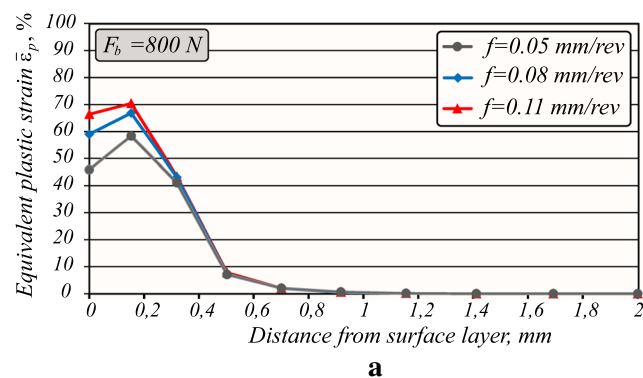
Fig. 4 Special STRB device

Table 3 X-ray specimens specification

Specimen's number	Type of finishing	Roller toroid radius r , mm	Burnishing force F_b , N	Number of passes n
1	Precision turning (reference conditions)	—	—	—
2	STRB	4	800	1
3			400	
4			1300	
5	2	800		
6	6			
7	4		6	

with the maximum at $2\theta \approx 139.5^\circ$. Diffraction profiles were fitted by the Pearson VII function, and lattice deformations were calculated. In the generalized Hooke's law, the Winholtz and Cohen method and X-ray elastic constants $s_1 = 4.89 \times 10^{-6} \text{ MPa}^{-1}$ and $\frac{1}{2}s_2 = 19.05 \times 10^{-6} \text{ MPa}^{-1}$ were applied. Moreover, the diffraction profile corresponding to Al {311} planes parallel to the surface was characterized by the full width at half maximum (FWHM) profile parameter, which could be interpreted as the “degree of plastic deformation”, because the diffraction profile broadening relates to such materials characteristics as grain size, microscopic residual stresses, or dislocation density, whose evolution is closely connected with plastic deformation. Parameters of the X-ray experiment were as follows: 2θ range of $134\text{--}144^\circ$, 2θ step of 0.4° , tilt defined by $\sin 2\psi = 0, 0.15, 0.3, 0.45$, and 0.6 of both positive and negative values of angle ψ . The maximum length of the irradiated area was $7 \mu\text{m}$.

Additionally, to validate the FE model, a specimen was subjected to STRB with a feed rate of $f = 0.05 \text{ mm/rev}$ and burnishing force of $F_b = 800 \text{ N}$, and the surface layers of the specimen were removed by electropolishing to measure the residual stress profile, according to recommendations given in [32].



3 FE results and discussion

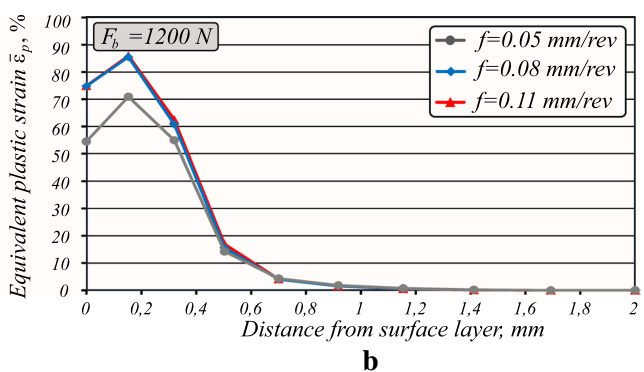
3.1 Equivalent plastic strain

The FE results for the equivalent plastic strain $\bar{\epsilon}_p$ distribution as a function of the burnishing force F_b and feed rate f are shown in Fig. 5. Increasing the burnishing force leads to a significant increase in the equivalent plastic strain $\bar{\epsilon}_p$ in the surface layer and, to a lesser extent, the depth of the plastically deformed zone. For the case of $F_b = 1200 \text{ N}$, compared to $F_b = 800 \text{ N}$, the maximum equivalent plastic strain $\bar{\epsilon}_p$ increases by $\approx 22\%$ and the plastic zone deepened by $\approx 0.25 \text{ mm}$. On the other hand, at a constant F_b , the equivalent plastic strain $\bar{\epsilon}_p$ decreases as the feed rate decreases. For all investigated variants, the maximum value of $\bar{\epsilon}_p$ is observed at a depth of $\approx 0.2 \text{ mm}$ from the surface layer. The burnishing force augmentation leads to a larger difference between the maximum value of the equivalent plastic deformation and the surface equivalent plastic deformation. Taking into account, the correlation between $\bar{\epsilon}_p$ and the microhardness, the maximum microhardness is likely to arise near the surface layer (within $\approx 0.2 \text{ mm}$).

3.2 Residual stresses

The FE results for the distribution of the hoop and axial residual stresses as a function of depth are summarized in Fig. 6. The following comments can be made:

- For a constant value of F_b , the feed rate f has a significant impact on the distribution of the hoop σ_t^{res} and axial σ_z^{res} residual stresses on the surface and at a particular depth. The study revealed opposite effects for the influence of f on the two types of residual stresses; with increasing of f , the surface residual hoop stresses σ_t^{res} decrease, and the residual axial stresses σ_z^{res} increase in absolute value. To maximize the axial residual stresses σ_z^{res} , it is appropri-

**Fig. 5** Equivalent plastic strain distribution

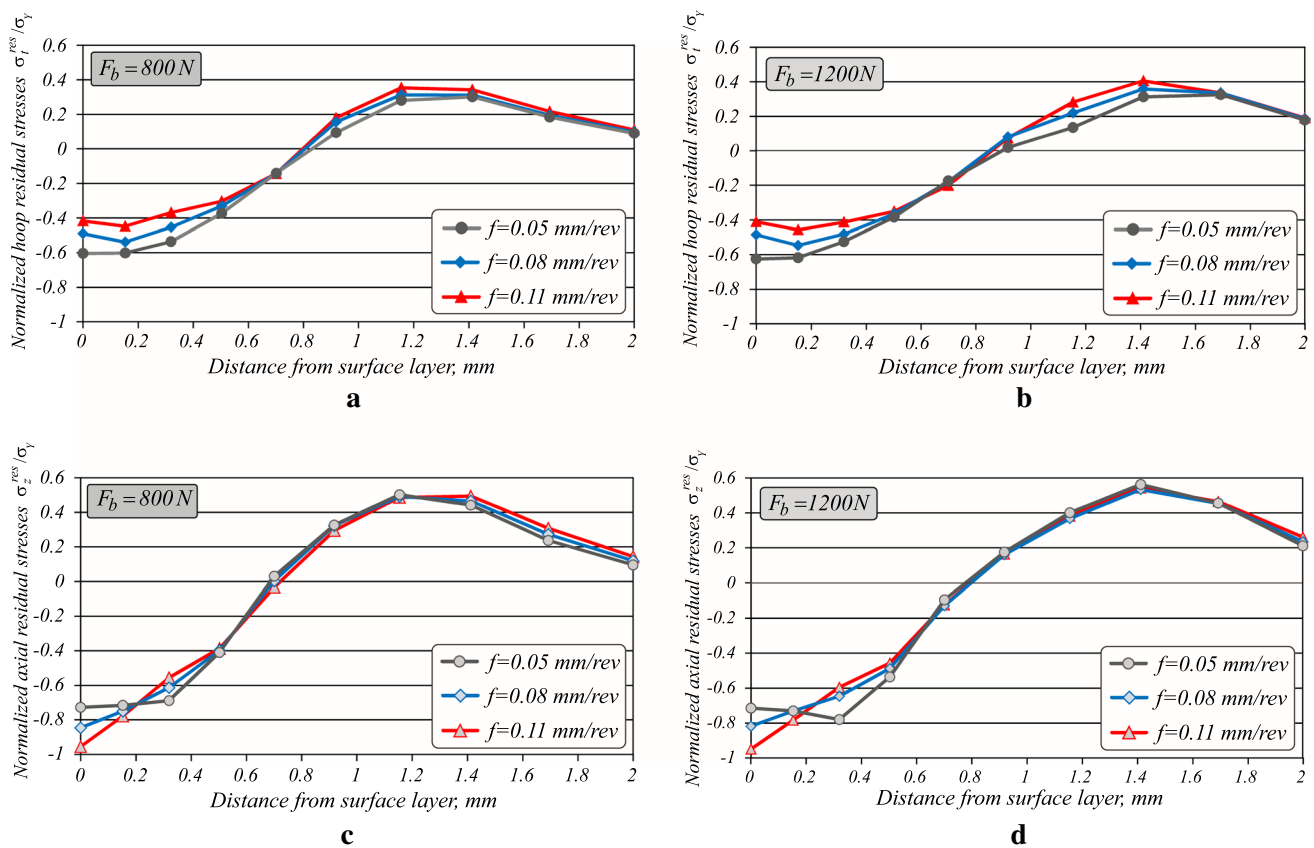


Fig. 6 FE residual stress distribution in a depth

ate to carry out the process with the maximum feed rate ($f = 0.11$ mm/rev).

- When the feed rate f is constant, the burnishing force F_b changes the hoop and axial residual surface stresses slightly. Also, F_b affects the distribution characteristics of the two types of residual stresses at a depth—increasing F_b leads to a relatively deeper compressive zone. An exception is observed in the distribution of the hoop residual surface stresses σ_t^{res} when the feed rate is the smallest ($f = 0.05$ mm/rev).

3.3 FE results validation

To validate the 3D FE model, a comparison was made between the FE results for the residual hoop σ_t^{res} and axial σ_z^{res} stress distribution and the experimentally measured distribution. X-ray diffraction stress analysis and electropolishing at a depth up to 0.4 mm from the surface layer were carried out. For this purpose, a cylindrical specimen of diameter $d = 22$ mm was subjected to STRB with process parameters in accordance with variant No. 2 from Table 2. Graphical visualization of the FE and experimental results for the hoop σ_t^{res} and axial σ_z^{res} residual stresses is shown in Fig. 7. The distributions of the two types of residual stresses are similar.

4 Experimental results and discussion

The X-ray diffraction analysis results for the surface axial σ_z^{res} and hoop σ_t^{res} residual stresses in the specimens (see Table 3) are shown in Fig. 8. The following comments can be made:

- Taking into account, the X-ray measurement error, it can be assumed that both types of residual stresses in specimen No. 1, processed only by turning (reference conditions), are negligibly small. Compared to specimen No. 1, significant compressive axial and hoop residual stresses were measured in the other samples treated via STRB. This proves the efficiency of the studied process in terms of the favorable macro-effect (the beneficial residual stresses introduced) in the 2024-T3 Al alloy.
- Regardless of the different combinations of r and F_b magnitudes, the axial residual stresses σ_z^{res} are higher than the hoop σ_t^{res} stresses in all specimens subjected to STRB. This corresponds to the results obtained via the validated 3D FE model.
- The specimens numbered 2, 3, and 4 were burnished with a constant value of the radius ($r = 4$ mm) but with varying values of the burnishing force. Taking into

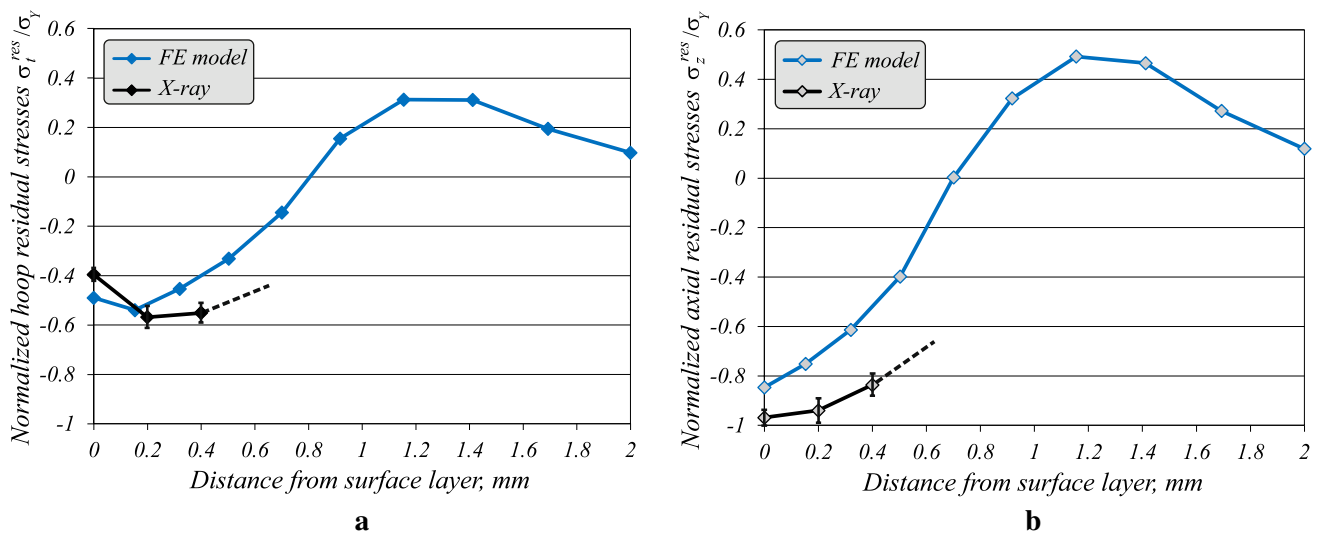


Fig. 7 Comparison of the residual stress distribution obtained via FE simulations and X-ray diffraction measurement

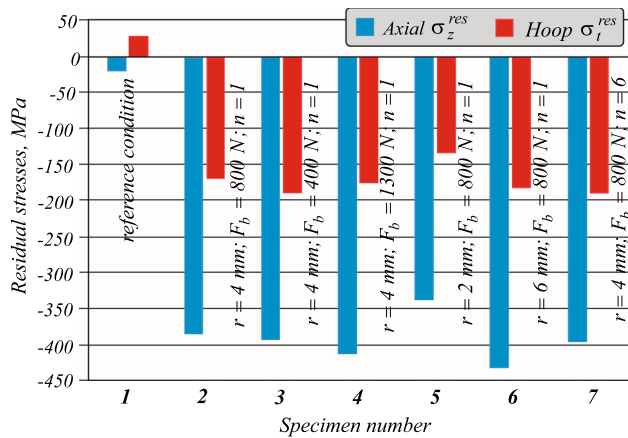


Fig. 8 Surface axial σ_z^{res} and hoop σ_t^{res} residual stresses

account, the X-ray diffraction technique error characteristic ($\Delta\sigma = 2 \div 33 \text{ MPa}$), the measured axial and hoop residual stresses are nearly equal and do not show a pronounced dependency on the burnishing force. The axial residual stress was the highest in the specimen No. 4 ($\sigma_z^{res} = -411 \text{ MPa}$), treated with the largest burnishing force ($F_b = 1300 \text{ MPa}$), and the smallest—in the specimen No. 2 ($\sigma_z^{res} = -386 \text{ MPa}$), treated with the average value of the burnishing force ($F_b = 800 \text{ MPa}$). The highest hoop residual stress was measured in specimen No. 3 ($\sigma_t^{res} = -189 \text{ MPa}$), treated with the least burnishing force.

- The specimens numbered 2, 5, and 6 were treated with a constant burnishing force ($F_b = 800 \text{ N}$) but with different toroid radii. The resulting axial and hoop residual stresses in this group of specimens show that a larger radius

increases both types of surface residual stresses in absolute value—the largest axial ($\sigma_z^{res} = -432 \text{ MPa}$) and hoop ($\sigma_t^{res} = -181 \text{ MPa}$) residual stresses were measured in specimen No. 6, which was treated with the largest radius ($r = 6 \text{ mm}$), and the smallest residual stresses were measured in specimen No. 5, treated with the smallest radius ($r = 2 \text{ mm}$).

- As in other static burnishing processes, this study included a roller toroid radius much larger than the feed rate values. As a consequence, in the direction of a generatrix from the workpiece cylindrical surface, the contact zones between the roller and the treated surface overlapped. As a result, even within a pass, the points from the surface layers are subjected to cyclic loading. For a workpiece with a specific material and diameter, the cyclic loading depends on the roller geometry, the feed rate, and the depth of penetration, respectively, on the burnishing force. Therefore, the different combinations of r and F_b cause different characteristics of strain hardening, the effect of which is expressed in the distribution of the axial and circumferential residual stresses on the surface and a particular depth.
- The results obtained for specimen No. 7, which was treated as specimen No. 2 but with six passes ($n = 6$), confirm the number of passes is a significant additional factor in creating a more pronounced zone with useful compressive residual stresses and, hence, fatigue life increasing.

5 Conclusions

FE analysis and experimental study of STRB of 2024-T3 Al alloy were conducted to evaluate the beneficial residual hoop and axial stresses. The following conclusions can be drawn:

- Using the flow stress concept, a 3D FE model was developed, and the actual STRB kinematics was simulated. The FE model was validated by comparing the FE results for hoop and axial residual stress distribution with values experimentally obtained via X-ray diffraction technique.
- The equivalent plastic strain in the surface layers increases when the feed rate increases at a constant burnishing force. This trend is observed up to a depth of ≈ 0.3 mm. The increase in burnishing force leads to an increase of the equivalent plastic strain in the surface layers.
- At a constant deforming force F_b , the feed rate f has an opposite effect on the surface axial residual stresses compared to the hoop residual stresses—in the $f = 0.05 \div 0.11$ mm/rev interval the increase in the feed rate leads to a decrease in the hoop residual stresses σ_t^{res} but an increase in the magnitude of the axial stresses σ_z^{res} . For all values of the feed rate, the burnishing force augmentation causes an increase in the compressive zone depth and slight increase in the surface residual stresses.
- The X-ray stress analysis results confirm the effectiveness of STRB of 2024-T3 Al alloy to introduce significant surface residual compressive axial and hoop stresses. It was proved that STRB implementation with six passes introduces greater magnitudes of surface residual stresses.

Acknowledgements This work was supported by the European Regional Development Fund within the OP “Science and Education for Smart Growth 2014–2020”, Project CoC “Smart Mechatronics, Eco- and Energy Saving Systems and Technologies”, No. BG05M2OP001-1.002-0023.

References

1. Maximov JT, Duncheva GV, Anchev AP, Ichkova MD (2019) Slide burnishing—review and prospects. *Int J Adv Manuf Technol* 104:785–801
2. Catalogue E (2006) Tools and solutions for metal surface improvement. Ecoroll Corporation Tool Technology USA
3. Maximov JT, Anchev AP, Dunchev VP, Ganev N, Duncheva GV, Selimov KF (2017) Effect of slide burnishing basic parameters on fatigue performance of 2024-T3 high-strength aluminium alloy. *Fatigue Fract Eng Mater Struct* 40(11):1893–1904
4. Maximov JT, Anchev AP, Duncheva GV, Ganev N, Selimov KF, Dunchev VP (2019) Impact of slide diamond burnishing additional parameters on fatigue behaviour of 2024-T3 Al alloy. *Fatigue Fract Eng Mater Struct* 42(1):363–373
5. Borkar AP, Kamble PS, Seemikeri CY (2014) Surface integrity enhancement of inconel 718 by using roller burnishing process. *Int J Curr Eng Technol* 4(4):2595–2598
6. Hassani-Gangaraj S, Carboni M, Gnagliano M (2015) Finite element approach toward an advanced understanding of deep rolling induced residual stresses, and an application to railway axles. *Mater Des* 83:689–703
7. Dwivedi SP, Sharma S, Mishra RK (2014) Effects of roller burnishing process parameters on surface roughness of A356/5%SiC composite using response surface methodology. *Adv Manuf* 2:303–317
8. Perenda J, Trajkovski J, Zerovnik A, Prebil I (2015) Residual stresses after deep rolling of a torsion bar made from high strength steel. *J Mater Process Technol* 218:89–98
9. Abrão AM, Denkena B, Köhler J, Breidenstein B, Mörke T (2014) The influence of deep rolling on the surface integrity of AISI 1060 high carbon steel. *Proc CIRP* 13:31–36
10. Chomienne V, Valiorgue F, Rech J, Verdu C (2016) Influence of ball burnishing on residual stress profile of a 15-5PH stainless steel. *CIRP J Manuf Sci Technol* 13:90–96
11. Yuan X, Sun Y, Li C, Liu W (2017) Experimental investigation into the effect of low plasticity burnishing parameters on the surface integrity of TA2. *Int J Adv Manuf Technol* 88:1089–1099
12. Zhang P, Lindemann J, Ding WJ, Leyens C (2010) Effect of roller burnishing on fatigue properties of the hot-rolled Mg–12Gd–3Y magnesium alloy. *Mater Chem Phys* 124:835–840
13. Fouad Y, Mhaede M, Wagner L (2010) Effect of mechanical surface treatment on fatigue performance of extruded ZK60 alloy. *Fatigue Fract Eng Mater Struct* 34:403–407
14. Wagner L, Mhaede M, Wollmann M, Altenberger I, Sano Y (2011) Surface layer properties and fatigue behavior in Al 7075-T73 and Ti–6Al–4V. Comparing results after laser peening, shot peening and ball-burnishing. *Int J Struct Integr* 2(2):185–199
15. Yen YC, Sartkulvanich P, Altan T (2005) Finite element modeling of roller burnishing process. *CIRP Ann Manuf Technol* 54(1):237–240
16. Sartkulvanich P, Altan T, Jasso F, Rodriguez C (2007) Finite element modeling of hard roller burnishing: an analysis on the effects of process parameters upon surface finish and residual stresses. *J Manuf Sci Eng* 129(4):705–716
17. Maximov JT, Anchev AP, Duncheva GV, Ganev N, Selimov KF (2017) Influence of the process parameters on the surface roughness, micro-hardness, and residual stresses in slide burnishing of high-strength aluminum alloys. *J Braz Soc Mech Sci Eng* 39(8):3067–3078
18. Maximov JT, Duncheva GV, Anchev AP, Ganev N, Amudjev IM, Dunchev VP (2018) Effect of slide burnishing method on the surface integrity of AISI 316Ti chromium–nickel steel. *J Braz Soc Mech Sci Eng* 40:194. <https://doi.org/10.1007/s40430-018-1135-3>
19. Maximov JT, Duncheva GV, Anchev AP, Ganev N, Dunchev VP (2019) Effect of cyclic hardening on fatigue performance of slide burnished components made of low-alloy medium carbon steel. *Fatigue Fract Eng Mater Struct* 42(6):1414–1425
20. Maximov JT, Duncheva GV, Anchev AP (2019) A temperature-dependent, non-linear kinematic/isotropic hardening material constitutive model of the surface layer of 37Cr4 steel subjected to slide burnishing. *Arab J Sci Eng* 44(6):5851–5862
21. Bougharriou A, Sai WB, Sai K (2010) Prediction of surface characteristics obtained by burnishing. *Int J Adv Manuf Technol* 51:205–215
22. Salahshoor M, Guo YB (2011) Finite element modeling of burnishing and the effects of process parameters on surface integrity of orthopedic implants. In: Proceedings of the ASME 2011 international mechanical engineering congress and exposition IMECE2011, November 11–17, Denver, Colorado, USA
23. Sayahi M, Sghaier S, Belhadjsalah H (2013) Finite element analysis of ball burnishing process: comparisons between numerical results and experiments. *Int J Adv Manuf Technol* 67:5–8
24. Hassanifard S, Mousavi M, Varvani-Farahani A (2018) The influence of low-plasticity burnishing process on the fatigue life of friction-stir-processed Al7075-T6 samples. *Fatigue Fract Eng Mater Struct* 42(3):764–772
25. Mohammadi F, Sedaghati R, Bonakdar A (2014) Finite element analysis and design optimization of low plasticity burnishing process. *Int J Adv Manuf Technol* 70:1337–1354

26. Zhuang W, Wicks B (2004) Multipass low-plasticity burnishing induced residual stresses: three-dimensional elastic–plastic finite element modeling. *Proc Inst Mech Eng Part C J Mech Eng Sci* 218(6):663–668
27. Aldrine ME, Mahendra Babu NC, Anil Kumara S (2017) Evaluation of induced residual stresses due to low plasticity burnishing through finite element simulation. *Mater Today Proc* 4:10850–10857
28. Balland P, Tabourot L, Degre F, Moreau V (2013) An investigation of the mechanics of roller burnishing through finite element simulation and experiments. *Int J Mach Tool Manuf* 65:29–36
29. Beghini M, Bertini L, Monelli BD, Santus S, Bandini M (2014) Experimental parameter sensitivity analysis of residual stresses induced by deep rolling on 7075-T6 aluminium alloy. *Surf Coat Technol* 254:175–186
30. Duncheva GV, Atanasov TP (2020) Finite element modeling and optimization of the deep rolling process with a torodal roller in aluminum alloy 2024 T3. *J Tech Univ Gabrovo* 60:3–14
31. Maximov JT, Duncheva GV, Anchev AP, Ichkova MD (2014) Modeling of strain hardening and creep behaviour of 2024-T3 aluminium alloy at room and high temperatures. *Comput Mater Sci* 83:381–393
32. Ganev N, Frydryšek K, Kolařík K (2007) Possibilities of FEM for verification of X-ray measurement of residual stresses depth distribution. In: *Book of extended abstracts. 9th international scientific conference applied mechanics 2007*. Technical University of Ostrava, Malenovice, April 16–19, 2007, pp 85–86, ISBN 978-80-248-1389-9

Publisher's Note Springer Nature remains neutral with regard to jurisdictional claims in published maps and institutional affiliations.